PHYSICAL REVIEW B **107**, 174403 (2023)

Ab initio statistical mechanics of the Néel transition in hexagonal YMnO$_3$: Antiferromagnetic domain walls, vortices, and local magnetoelectric coupling

Arpita Paul and Umesh V. Waghmare[*]
Theoretical Sciences Unit, Jawaharlal Nehru Centre for Advanced Scientific Research, Jakkur, Bangalore 560 064, India

(Received 24 March 2022; accepted 19 April 2023; published 4 May 2023)

Hexagonal manganites with coexisting antiferromagnetism and ferroelectricity have driven numerous research activities uncovering their potential in novel electronic devices. An antiferromagnetic order lowers the translational symmetry of the lattice; the structure of domain walls spatially separating distinctly ordered antiferromagnetic and structural states is quite rich and needs to be understood fundamentally. Here, we construct a model Hamiltonian to capture the low energy physics of coupled spins and phonons in hexagonal multiferroic YMnO$_3$ derived from first-principles density functional theory and determine its temperature dependent behavior using Monte Carlo simulations. We demonstrate a weakly first order or close to being second order Néel transition accompanied by a *giant* magnetoelastic effect observed experimentally in YMnO$_3$ and show how it originates from the coupling between the in-plane ordering of spins with symmetry of Γ_3 irreducible representation and collective atomic displacements with symmetry of Γ_1 irreducible representation. We reveal the intriguing magnetic structure with the symmetry of Γ_1 irreducible representation at the 180° antiferromagnetic domain wall and predict a linear magnetoelectric coupling which can be confirmed using the piezoresponse force microscopy. Finally, we show that a stable magnetic vortex forms along a line of intersection of six 60° antiferromagnetic domain walls, with energy comparable to that of dislocations in metals.

DOI: 10.1103/PhysRevB.107.174403

I. INTRODUCTION

Ferromagnetic materials have been the subject of great interest for centuries since the discovery of the first permanent magnet lodestone and its use as a compass [1]. The formation of lateral magnetic domain walls in ferromagnets is crucial for their applications in magnetic memory devices [2,3]. Magnetic domains are uniformly magnetized regions with the effective magnetization direction in a specific direction determined by local magnetic anisotropy [4,5]. Antiferromagnetism is another type of magnetic ordering that is commonly observed in many magnetic materials. It has been observed that many of the multiferroics and topological magnets (magnetic Weyl semimetals) are antiferromagnets [6–10]. Several exotic states with superconductivity and colossal magnetoresistance emerge from the antiferromagnetic state or a competition with it [11–13]. The absence of stray magnetic field in antiferromagnets makes them potential candidates for applications in spintronics [14,15]. In this context, understanding structure and dynamics of antiferromagnetic domains and domain walls at the microscopic level is fundamentally important [16,17]. Atomic spin structure at the domain walls in antiferromagnets has been investigated experimentally using spin-polarized scanning tunneling microscopy and x-ray photoemission microscopy [18,19] and has received renewed attention [20].

Modification of ferroic orders and their symmetry at domain walls results in rich physics and new functional properties which may not be envisaged in single domain bulk materials [21–25]. The discovery of electronic conductivity at the ferroelectric domain walls has opened a new avenue of research in understanding the mechanism and fabricating the domain walls based devices [21–25]. The domain walls in some ferromagnets exhibits topological Hall effects originating from magnetic skyrmions [26,27]. Recently, an unconventional anomalous Hall effect has been observed at the antiferromagnetic domain wall due to breaking of the local cubic symmetry [28]. Uncompensated magnetic moments at the coupled ferroelectric and antiferromagnetic domain walls have been experimentally detected in hexagonal ErMnO$_3$ [29].

Hexagonal rare earth manganites form an important class of materials with coexisting antiferromagnetic and structural-ferroelectric ordering [29–32]. Their high symmetry paraelectric phase undergoes a structural transition at a fairly high temperature involving unit cell tripling (through condensation of a zone boundary K_3 phonon mode) [30,33]. Ferroelectricity in these materials arises as a consequence of nonlinear coupling between this zone boundary (trimerization) instability and a zone-center polar mode as the secondary order parameter, making them improper ferroelectrics [33]. Furthermore, magnetic structure in hexagonal manganites is geometrically frustrated due to the antiferromagnetic coupling between the spins of Mn^{3+} ions on a triangular lattice [34]. This favors noncollinear ordering of spins that couples to phonons and strain [35,36], giving rise to rich physical phenomena such as giant magnetoelastic effect [36].

Among the hexagonal multiferroics, YMnO$_3$ is an extensively studied material with the coexistence of ferroelectricity ($T_C = 1270$ K) and antiferromagnetism ($T_N = 75$ K) [6,30,33]. It exhibits a spontaneous polarization of

---

[*] waghmare@jncasr.ac.in

6.5 μC/cm^2 [33] and six structural domains of distinct trimerized states arise below the structural transition temperature T_C, from condensation of a zone-boundary phonon [6,30]. Landau theory with inputs from first principles has been used effectively to understand the nature of structural and ferroelectric domain walls in hexagonal manganites [6,37]. Boundaries between the six structurally ordered domains can intersect at a line forming a topological defect, which has been observed with conducting force and transmission electron microscopy [38–40]. Polarization changes sign across a structural domain wall in the topological defect state due to the *improper* nature of ferroelectricity [6,40]. Recently, stable and sharp charged ferroelectric domain walls have also been characterized experimentally in single crystal of improper ferroelectric YMnO$_3$ [41,42].

The spin texture across an antiferromagnetic domain wall below T_N and the nature of magnetic transition in YMnO$_3$ are yet to be investigated. It was inferred from neutron diffraction experiments [43,44] that the magnetic moments of Mn^{3+} ions order antiferromagnetically (noncollinear ordering) in the *ab* plane according to Γ_3 irreducible representation below 75 K, without reducing the structural symmetry further [36]. Yet Néel transition is accompanied by a distinct anomaly in the structure, i.e., cell parameters and atomic positions, which was termed as the *giant* magnetoelastic effect [36]. The coupling of spins with Γ_1 phonons was believed to be responsible for the observed *giant* magnetoelastic effect using neutron diffraction experiments [36], which was corroborated by first-principles calculations [45]. It was speculated earlier [6] that the experimentally observed structural vortices (topological defects) in LuMnO$_3$ are also magnetic vortices due to the microscopic coupling between the tilting angle of the MnO$_5$ bipyramid and the axis of in-plane magnetocrystalline anisotropy. However, the symmetry of the magnetic ground state of LuMnO$_3$ is Γ_4, while that of YMnO$_3$ is Γ_3. It is intriguing and important to understand if and how symmetry of the magnetic ground state influences the nature of antiferromagnetic domains and topological defects.

In this work, we determine the temperature dependent behavior of antiferromagnetic and structural order parameters relevant to Néel transition in YMnO$_3$ using statistical mechanical analysis of a first-principles model Hamiltonian. We highlight the role of spin-phonon coupling in atomic scale structure of magnetostructural domain walls and develop an understanding of how antiferromagnetic and structural domains are locked below T_N. We predict a nontrivial linear magnetoelectric coupling at the 180° antiferromagnetic domain wall which can be utilized in its visualization in experiment. We show that structural vortex state in YMnO$_3$ is locked to magnetic vortex state below Néel temperature.

II. RESULTS AND DISCUSSION

A. Symmetry of magnetic and structural order parameters

Earlier first-principles calculations [45] on YMnO$_3$ have corroborated the experimental finding that an antiferromagnetic state with ordering of spins of Mn^{3+} in the *ab* plane [first magnetic basis vector; see Fig. 1(a)] according to Γ_3 irreducible representation (parent ferroelectric and paramagnetic space group: $P6_3cm1'$) has the lowest energy. Surprisingly, the magnetic state with the same symmetry and spins ordered along the z axis (M; see Fig. S2 in [48]), corresponding to another magnetic basis vector of Γ_3 irreducible representation ($P6_3cm1'$ space group) has a notably higher energy [45]. A large energy difference (86 meV/f.u.) between these two isosymmetric states originates mainly from energies associated with strong in-plane superexchange interaction and easy plane magnetocrystalline anisotropy [45].

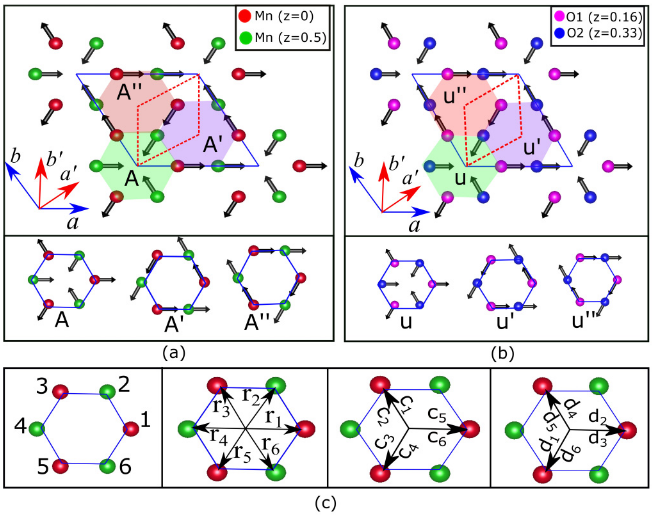

FIG. 1. (a) In-plane magnetic ordering of spins (of Mn atoms) according to the symmetry of Γ_3 irreducible representation and (b) in-plane displacements of apical oxygen (O1 and O2) atoms according to Γ_1 irreducible representation of the ferroelectric and paramagnetic $P6_3cm1'$ phase. a and b (a' and b') represent lattice unit cell vectors of the ferroelectric (paraelectric) structure. A, A', and A'' in (a) are the local magnetic order parameters defining spin orientations of Mn atoms in a hexagonal cluster. u, u', u'' in (b) are the local structural order parameters defining apical oxygen displacements (structural states) with respect to the ferroelectric and paramagnetic $P6_3cm1'$ phase. A's (u's) are essentially the spin (lattice) Wannier functions which form a localized basis that spans the subspace of the effective Hamiltonian. $-A$, $-A'$, and $-A''$ magnetic states are obtained by applying time reversal symmetry operation on the A, A', and A'' states, respectively. Similarly, $-u$, $-u'$, and $-u''$ structural states are obtained from u, u', and u'' structural states by applying spatial inversion symmetry. The radial vectors r_i, c_i ($r_i = c_{(i-1)\mathrm{mod}6}$ and $c_{(i-2)\mathrm{mod}6}$, for odd i), and d_i ($r_i = d_{i+1}$ and d_{i+2}, for odd i) defined in (c) are used to determine the local antiferromagnetic order parameters A, A', and A'' [see Eq. (1) in the text] in a unit cell consisting of six Mn atoms ($i = 1, 2, 3, \ldots, 6$). Among the three choices of hexagons in the unit cell [green, purple, and red in Fig. 1(a)], the green hexagon is used in estimating the local antiferromagnetic order parameters.

Translational symmetry operations $R_{a'}$ and $R_{b'}$ (symmetry elements of the high symmetry paraelectric and paramagnetic phase $P6_3/mmc1'$, $T > T_C$) transform the antiferromagnetically ordered state A_Γ to A''_Γ and A'_Γ [see Fig. 1(a) and Table I], respectively. Six energetically equivalent antiferromagnetic states—(a) A_Γ, $-A_\Gamma$, (b) A'_Γ, $-A'_\Gamma$, and (c) A''_Γ, $-A''_\Gamma$ [see Fig. 1(a)]—emerge from a combination of translational and time reversal operations on the antiferromagnetic state A_Γ. On the other hand, the isosymmetric antiferromagnetic state

TABLE I. Transformations of order parameters of magnetic (A_Γ's and M), structural (u_Γ's), and ferroelectric (P_z) states under the relevant symmetry operations. Antiferromagnetic ordering according to Γ_3 irreducible representation of ferroelectric and paramagnetic $P6_3cm1'$ space group is formed by $A_\Gamma = \sum_{\vec{R}} A(\vec{R})$ ($\vec{R} = \mathrm{n}\vec{a} + \mathrm{m}\vec{b}$ denote lattice vectors of the ferroelectric lattice), $A'_\Gamma = \sum_{\vec{R}} A'(\vec{R})$, and $A''_\Gamma = \sum_{\vec{R}} A''(\vec{R})$. A ($\vec{R}$), A' ($\vec{R}$), and A'' ($\vec{R}$) represent the localized basis of antiferromagnetic order parameters [see Fig. 1(a)]. Apical oxygen displacements according to the symmetry of Γ_1 irreducible representation of the ferroelectric and paramagnetic $P6_3cm1'$ space group are defined by $u_\Gamma = \sum_{\vec{R}} u(\vec{R})$, $u'_\Gamma = \sum_{\vec{R}} u'(\vec{R})$, and $u''_\Gamma = \sum_{\vec{R}} u''(\vec{R})$. u ($\vec{R}$), u' ($\vec{R}$), and u'' ($\vec{R}$) represent the localized basis of structural order parameters; see Fig. 1(b). a' and b' represent lattice vectors of the paraelectric lattice ($P6_3/mmc1'$ space group).

Order parameter	$R_{a'}$ (Translation)	$R_{b'}$ (Translation)	I (Spatial inversion)	τ (Time reversal)
A_Γ	A''_Γ	A'_Γ	A_Γ	$-A_\Gamma$
M	M	M	M	$-M$
u_Γ	u''_Γ	u'_Γ	$-u_\Gamma$	u_Γ
P_z	P_z	P_z	$-P_z$	P_z

M ($P6_3cm1'$ space group; see Table I here and Fig. S2 in [48]) remains unaltered under the translational symmetry operations R'_a and R'_b (see Table I) as it involves antiferromagnetic ordering of spins along the z axis.

Earlier experimental measurements and first-principles theoretical analysis [36,45] have demonstrated that the atomic displacements in the ferroelectric phase ($P6_3cm1'$ space group) corresponding to Γ_1 irreducible representation [u's; see Fig. 1(b) here and Fig. S1(f) in [48]] couple strongly with spins. u_Γ's represent atomic displacements [giving structural states of Γ_1 irreducible representation; see Fig. 1(b)] taken with respect to their positions in the ferroelectric and paramagnetic phase ($P6_3cm1'$ space group). Group theoretical analysis [46] shows that experimental [36] atomic displacements in YMnO$_3$ corresponding to Γ_1 irreducible representation of $P6_3cm1'$ space group [involved in structural distortion at Néel transition; see Fig. 1(b)] are compatible with the atomic displacements of zone boundary polar K_3 (see Fig. S1(a)-S1(d) in [48], tilting of MnO$_5$ bipyramids, and out of plane displacements of Y and equatorial O atoms) and nonpolar K_1 (see Fig. S3(a)-S3(b) in [48], in-plane displacements of Mn, and apical O atoms) phonon modes and zone center polar Γ_2^- phonon mode (out of plane displacements of all atoms) of the paraelectric and paramagnetic phase ($P6_3/mmc1'$ space group; see Table II). In contrast, atomic displacements of only K_1 mode are shown to be involved in spin reorientation transition in hexagonal LuFeO$_3$ [47], which is isostructural to paraelectric hexagonal YMnO$_3$. Our first-principles calculations of the structure of antiferromagnetic YMnO$_3$ involves K_3 and Γ_2^- modes with amplitudes comparable to their experimental values [36] (see Table II). However, the amplitude of the K_1 phonon mode is severely underestimated (by a factor of eight) in our analysis in comparison with experiment (see Table II here and Sec. E in [48]). This is consistent with recent findings [49,50] that the first-principles predictions of positions of Mn atoms in the antiferromagnetic YMnO$_3$ are close to their experimental positions [36] at room temperature (i.e., small amplitude of K_1 phonon mode). While we thus associate u_Γ's (structural states defining localized atomic displacements according to Γ_1 irreducible representation of ferroelectric $P6_3cm1'$ space group) here primarily to polar K_3 (see Fig. S1(a)-S1(c) in [48]) and Γ_2^- phonon modes of paraelectric phase ($P6_3/mmc1'$ space group), its discrepancy with respect to experiment (K_1 mode) is an open question and needs more work.

Translation (by R'_a and R'_b of the paraelectric unit cell) and spatial inversion operations on u_Γ result in six distinct structural states $\pm u_\Gamma$, $\pm u'_\Gamma$, and $\pm u''_\Gamma$ [see Fig. 1(b)]. The experimentally observed displacements [36] of apical oxygen atoms in the ferroelectric $P6_3cm1'$ phase (Γ_1 irreducible representation) near Néel transition occur in the same direction [51] (see Table S1 in [48]) as the apical oxygen displacements leading to trimerization of the paraelectric unit cell (K_3 irreducible representation of paraelectric $P6_3/mmc1'$ space group). As the K_3 and Γ_2^- polar phonon modes of paraelectric $P6_3/mmc1'$ phase couple nonlinearly ($u_{K_3}^3 u_{\Gamma_2^-}$), polarization (P_z) changes its sign if directions of apical oxygen displacements associated with zone boundary K_3 phonon mode reverse [6,37]. Thus u_Γ's and $-u_\Gamma$'s structural states (displacements of apical oxygen atoms according to the symmetry of Γ_1 irreducible representation of ferroelectric $P6_3cm1'$ space group) appear in the ferroelectric phase with positive and negative values of polarization (P_z), respectively [51]. This is in agreement with experimental findings [51] that the magnitude of ferroelectric polarization increases significantly below T_N. Structural states (u_Γ's) corresponding to Γ_1 irreducible representation of ferroelectric $P6_3cm1'$ space group transform in a manner similar to polar K_3 and Γ_2^- phonon modes (polarization P_z) of the paraelectric $P6_3/mmc1'$ space group under the spatial inversion operation (see Table I). Therefore, the six structural

TABLE II. Projection of atomic displacements according to the symmetry of Γ_1 irreducible representation involved in structural distortions at the Néel transition, taken with respect to the low temperature ferroelectric and paramagnetic $P6_3cm1'$ phase, on the basis vectors of K_1, K_3, and Γ_2^- phonon modes of the high temperature paraelectric, paramagnetic $P6_3/mmc1'$ phase. R's represent atomic positions.

Atomic displacement (Γ_1)	K_1	K_3	Γ_2^-
$R_{\rm ion}^{300\,\rm K}$ (Expt. [36]) - $R_{\rm ion}^{10\,\rm K}$ (Expt. [36])	0.66	0.62	0.52
$R_{\rm ion}^{300\,\rm K}$ (Expt. [36]) - $R_{\rm ion}^{0\,\rm K}$ (LDA+SOC, Γ_3 AFM ordering)	0.08	0.35	0.89

states, u_Γ's, of ferroelectric $P6_3cm1'$ phase [Γ_1 irreducible representation; see Fig. 1(b)] correspond to the six trimerized structural states (see Fig. S1(a)-S1(c) in [48]). Correlations of u_Γ's [Γ_1 irreducible representation of ferroelectric $P6_3cm1'$ space group; see Fig. 1(b)] with polar K_3 (trimerization angle Φ; see Fig. S1(a)-S1(c) in [48]) and Γ_2^- (P_z) phonon modes of a paraelectric $P6_3/mmc1'$ phase [6,37] are given as (a) $\Phi = 0(\alpha^+, +P_z) \rightarrow u_\Gamma$, (b) $\Phi = \pi(\alpha^-, -P_z) \rightarrow -u_\Gamma$, (c) $\Phi = 2\pi/3(\beta^+, +P_z) \rightarrow u'_\Gamma$, (d) $\Phi = -\pi/3(\beta^-, -P_z) \rightarrow -u'_\Gamma$, (e) $\Phi = -2\pi/3(\gamma^+, +P_z) \rightarrow u''_\Gamma$, and (f) $\Phi = \pi/3(\gamma^-, -P_z) \rightarrow -u''_\Gamma$.

Change in the axis of in-plane magnetocrystalline anisotropy [i.e., change in the antiferromagnetic ordering from A_Γ to A'_Γ; see Fig. 1(a)] results from a change in in-plane displacements of apical oxygen atoms [u_Γ to u'_Γ, Γ_1 irreducible representation of $P6_3cm1'$ space group; see Fig. 1(b)] through the third order spin-phonon coupling [6]. Hence structural states (u_Γ, u'_Γ, and u''_Γ) are locked to the antiferromagnetic states (A_Γ, A'_Γ, and A''_Γ). When A_Γ transforms to A''_Γ and A'_Γ upon translations by $R_{a'}$ and $R_{b'}$, u_Γ correspondingly changes to u''_Γ and u'_Γ (see Table I). These antiferromagnetic states (A_Γ, A'_Γ, and A''_Γ) or the basis vectors of Γ_3 magnetic representation [in Fig. 1(a) here and Fig. S2 in [48]] are constituted of the localized basis of the primary order parameters of the Néel transition: A, A', A'', and M in the unit cell, which are especially spin Wannier functions, defined as

$$A = \frac{1}{6}\sum_{i=1}^{6}(-1)^i(\hat{r}_i \cdot \hat{s}_i), \quad A' = \frac{1}{6}\sum_{i=1}^{6}(\hat{c}_i \cdot \hat{s}_i),$$
$$A'' = \frac{1}{6}\sum_{i=1}^{6}(\hat{d}_i \cdot \hat{s}_i), \quad M = \frac{1}{6}\sum_{i=1}^{6}(-1)^i s_{i,z}, \tag{1}$$

where $\hat{r}_i$ represents a unit vector along the in-plane projection of the position vector of ith Mn atom [$i = 1, \ldots, 6$; see Fig. 1(c)] with respect to the center [$\sum_{i=1}^{6}\hat{r}_i = 0$; see Fig. 1(c)] and $s_{i,z}$ is the z component of $\hat{s}_i$ (spin vector of ith Mn atom). $\hat{c}_i$ and $\hat{d}_i$ are sets of radial vectors [$\sum_{i=1}^{6}\hat{c}_i = \sum_{i=1}^{6}\hat{d}_i = 0$; see Fig. 1(c)]. The secondary order parameters relevant to the Néel transition are the atomic displacements (u_Γ, u'_Γ, and u''_Γ form a localized basis) with the symmetry of Γ_1 irreducible representation ($P6_3cm1'$ space group).

B. Model Hamiltonian

To capture the low energy landscape of primary (A, A', A'', and M) and secondary (u, u', and u'') order parameters governing the Néel transition, we consider a coupled lattice-spin Hamiltonian involving terms contributed by spins [45] and atomic displacements (Γ_1 symmetry):

$$\begin{aligned} H = {} & J_p \sum_{\langle ij\rangle,P} \hat{s}_i \cdot \hat{s}_j + J_{ip} \sum_{\langle ij\rangle,IP} \hat{s}_i \cdot \hat{s}_j + K_p \sum_i \sin^2\theta_i \\ & + K_a \sum_i \left\{ (\hat{r}_i \cdot \hat{s}_i)^2 + \sum_i (\hat{c}_i \cdot \hat{s}_i)^2 + \sum_i (\hat{d}_i \cdot \hat{s}_i)^2 \right\} \\ & + \frac{1}{2} U k \left(u_\Gamma^2 + u_\Gamma'^2 + u_\Gamma''^2\right) \\ & + \alpha \sum_{n=1}^{U} \left(A_n^2 u_\Gamma + A_n'^2 u'_\Gamma + A_n''^2 u''_\Gamma\right), \end{aligned} \tag{2}$$

where J_p and J_{ip} are the coefficients of in-plane and interplane superexchange interaction between nearest neighbor Mn^{3+} spins, respectively, θ_i is the angle between spin $\hat{s}_i$ and z axis, K_p and K_a are constants of easy plane (confining spins in the ab plane) and in-plane easy axis [constrains $\hat{s}_i$'s along $\hat{r}_i$'s and $\hat{c}_i$'s and $\hat{d}_i$'s in the ab plane; see Fig. 1(c)] magnetocrystalline anisotropy, respectively, k is the spring constant associated with the phonon mode of Γ_1 irreducible representation, and α is the third-order spin-phonon coupling constant. $\{A_n\}$ is the value of the order parameter $\{A\}$ in the nth unit cell ($n = 1$ to U; U is the total number of unit cells) and i (j) vary from 1 to $6U$ spins. We consider a symmetry allowed coupling (third order) between uniform order parameters, the Γ_1 phonon mode (compatible with K_3 and Γ_2^- phonon modes of the paraelectric $P6_3/mmc1'$ phase) and local magnetic ordering, microscopic coupling [52] that leads to the imbalance in nearest neighbor superexchange interactions. Values of parameters $J_p = 18$ meV, $J_{ip} = 0.07$ meV, $K_P = -4$ meV, and $K_a = -0.3$ meV were estimated using energies of several noncollinearly ordered antiferromagnetic states simulated within first-principles density functional theory [45]. While coupling of u_Γ's with A_Γ's and M are allowed by symmetry, the relevance of coupling between u_Γ's and M is not significant as the M state is much higher in energy (86 meV/f.u. [45]) than the A_Γ state (from the results of first-principles calculations [45]). Minimizing H [Eq. (2)] with respect to u_Γ, u'_Γ, and u''_Γ we get

$$\begin{aligned} u_{\Gamma,\min} &= -\frac{\alpha}{k}\sum_n A_n^2, \\ u'_{\Gamma,\min} &= -\frac{\alpha}{k}\sum_n A_n'^2, \\ u''_{\Gamma,\min} &= -\frac{\alpha}{k}\sum_n A_n''^2. \end{aligned} \tag{3}$$

Our first-principles DFT calculations predict that atomic positions in the antiferromagnetically ordered state with the symmetry of Γ_3 irreducible representation (A_Γ state) are close to their values in the paramagnetic state (see Table II and Table S1 in [48]) and suggest a weak spin-phonon coupling constant. Atomic positions of the paramagnetic and antiferromagnetic states reported earlier are very dispersed and there is no consensus yet particularly on the positions of Mn atoms (see Table S2 and Sec. E in [48]). We determine the strength of a third order spin-phonon coupling constant (α) by considering experimental crystal structures [36] at 300 K (crystal structure in paramagnetic state) and 10 K (crystal structure in antiferromagnetically ordered state). Here u_Γ's represent the experimental atomic displacements from their positions in the paramagnetic and ferroelectric $P6_3cm1'$ phase (above T_N) [36]. Our first-principles calculations reveal that the antiferromagnetically ordered state with the symmetry of Γ_3 irreducible representation (A_Γ state) at the 10 K experimental structure is 40 meV/f.u. higher than that with experimental crystal structure at 300 K (which is close to the DFT ground state). Our estimated magnitude of u is around 0.014 Å (see Fig. S4(a)-S4(b) in [48]) which is six times smaller than its experimental value [36]. These results highlight that spin-phonon coupling is *underestimated* in first-principles local DFT calculations (see Table II here, and Table S2 and

Fig. S4 in [48]). The estimate of $\frac{\alpha^2}{2k}$ ($= \frac{6}{U}$ meV, where U is the number of unit cells) is obtained from the third order spin-phonon coupling constant ($\alpha = -0.99$ eV/Å) associated with the experimentally measured atomic displacements with Γ_1 symmetry (see Fig. S4(b) and Sec. E in [48]). Integrating out u_Γ's, the renormalized spin Hamiltonian (H_R) is

$$H_R = J_p \sum_{\langle ij\rangle,P} \hat{s}_i \cdot \hat{s}_j + J_{ip} \sum_{\langle ij\rangle,IP} \hat{s}_i \cdot \hat{s}_j + K_p \sum_i \sin^2\theta_i + K_a\left(\sum_i (\hat{r}_i\cdot\hat{s}_i)^2 + \sum_i (\hat{c}_i\cdot\hat{s}_i)^2 + \sum_i (\hat{d}_i\cdot\hat{s}_i)^2\right) - \frac{\alpha^2}{2k}\left[\left(\sum_{n=1}^{U} A_n^2\right)^2 + \left(\sum_{n=1}^{U} A'^2_n\right)^2 + \left(\sum_{n=1}^{U} A''^2_n\right)^2\right]. \quad (4)$$

We note that the local antiferromagnetic (A_Γ's) order parameters are linearly dependent: $A_\Gamma = -A'_\Gamma$-A''_Γ [see Figs. 1(a) and 1(b) and Eq. (1)]. In contrast, the trimerized structural state [see Figs. 1(b) and S1a-c] [α^+ ($\Phi = 0$), $+P_z$] cannot be expressed as a linear combination of [γ^- ($\Phi = \pi/3$), $-P_z$] and [β^- ($\Phi = -\pi/3$), $-P_z$] trimerized structural states since the sign of polarization (P_z) changes in the last two. Similarly the structural state u_Γ [α^+ ($\Phi = 0$), $+P_z$] cannot be expressed in terms of $-u''_\Gamma$ [γ^- ($\Phi = \pi/3$), $-P_z$] and -u'_Γ [β^- ($\Phi = -\pi/3$), $-P_z$] since the parent ferroelectric structures corresponding to u_Γ and $-u'_\Gamma$ have opposite sign of polarization. We set the spin-phonon coupling parameter $\frac{\alpha^2}{2k}$ to $\frac{6}{U}$ (U is the total number of ferroelectric unit cells) when the first component of the last term (one structural state) in Eq. (4) is considered (Secs. II C and II D). In a homogeneously ordered magnetic state A_Γ, an additional component of energy contributed by A'_Γ and A''_Γ ($A_\Gamma = -A'_\Gamma - A''_\Gamma$; $A = 1$, $A' = -0.5$, and $A'' = -0.5$) arises if all three components of the last term in Eq. (4) are considered. We then renormalize the spin-phonon coupling parameter $\frac{\alpha^2}{2k}$ to $\frac{5.3}{U}$ to account for the additional energy contribution [all three components of the last term in Eq. (4), Secs. II E and II F].

We perform heating-up and cooling-down classical Monte Carlo simulations of the renormalized spin Hamiltonian with periodic boundary conditions.

C. Néel phase transition

We first discuss results of Monte Carlo simulations of the model Hamiltonian that considers [first components of the fourth and fifth terms in addition to the first three terms in Eq. (4)] only one structural state u_Γ [see Eq. (2)]. We determine antiferromagnetic and structural order parameters A, M, and u [in the green hexagon of Figs. 1(a) and 1(b)] at each temperature using Eq. (1) and Eq. (3). Order parameter M [see Eq. (1)] involving antiferromagnetic ordering of spins along the z axis remains close to zero at low temperatures [see Fig. 2(a)] since the spins are confined mostly to the xy plane (see Fig. S5 in [48]). Our estimate of T_N is 92 K, which is in reasonable agreement with its experimental [43] value of 75 K. Aniferromagnetic order parameter A below T_N induces a nonzero value of the secondary structural order parameter u [using Eq. (3)]. Thus it corroborates that spin-phonon coupling (α) constitutes the microscopic mechanism of the experimentally observed *giant* magnetoelastic effect below $T < T_N$ [36]. Specific heat (C_V) and magnetic susceptibility (χ) exhibit peaks near T_N [see Figs. 2(c) and 2(d)], further confirming the existence of the Néel transition. The absence of thermal hysteresis in order parameters, temperature dependence of C_V, and magnetic susceptibility near T_N [see Figs. 2(a), 2(c) and 2(d)] obtained from heating-up and cooling-down simulations suggest the second-order nature of the Néel transition. The in-plane components of magnetic susceptibility remain larger at all temperatures compared to its out-of-plane component, in agreement with experiment [53]. This anisotropy in in-plane and out-of-plane magnetic susceptibilities emerges from the magnetocrystalline anisotropy and spin-phonon coupling terms which elucidate the experimentally observed anisotropy in magnetic susceptibility [53]. Our estimate of the Curie Weiss temperature (θ_{CW}) from the high temperature behavior of the in-plane component of inverse susceptibility (well above T_N; see Fig. S6 in [48]) is ~ -720 K, which is comparable to its experimental estimate [53]. We find similar results when the full Hamiltonian [see Eq. (4)] with multiple structural and magnetic domains (see Fig. S7 in [48]) is considered in our simulations. Magnetic states with symmetry of Γ_2 and Γ_3 irreducible representations both appear at low temperature in the absence of spin-phonon coupling [third order coupling; last term in Eq. (2) here and see Figs. S8(a) and S9(a)-S9(c) in [48]]. Spin-phonon coupling [see Eq. (2)] effectively lowers the energy of the magnetic state corresponding to Γ_3 irreducible representation relative to the competing magnetic state corresponding to Γ_2 irreducible representation [see Figs. 2(a) here and S8(a)-S8(b) in [48]].

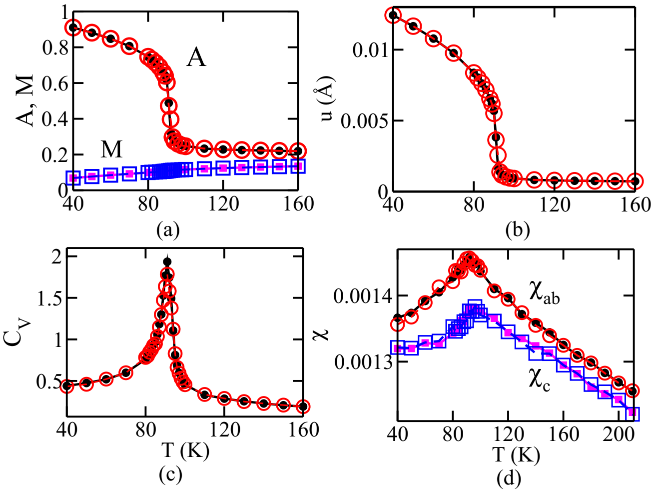

FIG. 2. Temperature dependent variations in (a) antiferromagnetic order parameters (A and M), (b) structural change of Γ_1 symmetry (u), (c) specific heat (C_V), and (d) magnetic susceptibilities. Results of heating and cooling simulations are represented with solid (filled symbols) and dashed lines (hollow symbols), respectively. Values of antiferromagnetic order parameters A' and A'' (arising from linear dependency; see Sec. II B) are restricted to $|A'| = |A''| = \frac{|A|}{2}$ at all temperatures.

Relatively small magnitude of u (0.014 Å at 10 K) estimated from Monte Carlo simulations is attributed to the underestimation of spin-phonon coupling in first-principles calculations (see Sec. II A, Table II here, and Sec. E in [48]) and also the deficiency of DFT calculations of the K_1 component of the structure of the antiferromagnetic ground state. The third order spin-phonon coupling [see Eq. (2) and Eq. (4)] manifests itself in long range coupling between spins and hence a first-order transition is expected. When we increase the spin-phonon coupling parameter ten times ($\frac{\alpha^2}{4k} = \frac{60}{U}$ meV), we find notably large atomic displacements, though still underestimated by a half relative to its experimental value (0.09 Å). We observe a first-order Néel transition at a higher temperature (∼120 K) when the spin-phonon coupling is significantly enhanced (see Fig. S8(a)-S8(c) in [48]). Therefore, we conclude that the Néel transition in $\mathrm{YMnO_3}$ is weakly first order or close to being second order in nature. Additionally quantum spin fluctuations play an important role in frustrated magnetic systems [54] and the signature of spin fluctuations has been observed in neutron diffraction measurements in hexagonal $\mathrm{YMnO_3}$ [55]. Dynamical mean field theoretical methods, which treat dynamical electronic correlations, have recently been shown to predict crystal structures of strongly correlated materials (transition metal oxides) more accurately compared to methods like local DFT that include static electronic correlations [56]. Density functional theory does not incorporate the effects of quantum spin fluctuations [57,58] and dynamical electronic correlations [56], which probably have a contribution to the third order spin-phonon coupling constant (not captured in our first-principles simulations, i.e., the position of the Mn atom is close to its value in the paramagnetic state), and it will encourage further studies in future.

D. 180° antiferromagnetic domain walls

We now discuss spatially inhomogeneous ordering into antiferromagnetic domains and the spin texture at the magnetic domain walls at low temperature ($T < T_N$). The antiferromagnetic states A_Γ [see Fig. 3(a)] and $-A_\Gamma$ are symmetry equivalent and are related by time reversal symmetry. To determine the ordering of spins at the 180° magnetic domain wall (spins effectively rotate by 180° across a domain wall separating A_Γ and $-A_\Gamma$), we simulated the model Hamiltonian [Eq. (4)] restricting to a single structural state (u_Γ and corresponding antiferromagnetic states A_Γ and $-A_\Gamma$) with a periodic system of 40 × 40 × 8 unit cells (76 800 spins). We obtain a configuration (through heating-up Monte Carlo simulation with initial state having a stripe domain pattern formed of two antiferromagnetic states A_Γ and $-A_\Gamma$ in the *ab* plane) with stripes of domains of antiferromagnetic orderings (A_Γ and $-A_\Gamma$) at 4 K [see Fig. 3(a)]. The width of the simulated 180° antiferromagnetic domain wall is about 24–30 Å (four–five unit cells thick), which is comparable to that of a calculated antiferromagnetic domain wall (40–90 Å) in hexagonal $\mathrm{LuMnO_3}$ [6]. The width of 180° antiferromagnetic domain wall (24–30 Å) in $\mathrm{YMnO_3}$ is comparable to the widths of ferroelectric domain walls in $\mathrm{BaTiO_3}$ (30 Å thick 90° domain wall [59]) and $\mathrm{PbZr_{0.2}Ti_{0.8}O_3}$ (70 Å thick 180° domain wall [24]). However, it is much smaller than earlier estimates for 180° magnetic domain walls in collinear antiferromagnet NiO (1500 Å [60]), $\mathrm{Cr_2O_3}$ (420–650 Å [61]), and ferromagnet $\mathrm{La_{0.7}Ca_{0.3}MnO_3}$ (380 Å [62]). Our estimate of the domain wall energy is 4 $\mathrm{mJ/m^2}$, which is an order of magnitude higher than that associated with an antiferromagnetic domain wall at the surface of NiO (0.42 $\mathrm{mJ/m^2}$) [60,63]. It is comparable to the theoretical estimates of 180° ferroelectric domain wall energy in improper ferroelectric $\mathrm{YMnO_3}$ (11 $\mathrm{mJ/m^2}$) [37] and proper ferroelectric $\mathrm{BaTiO_3}$ (6–16 $\mathrm{mJ/m^2}$) [59,64].

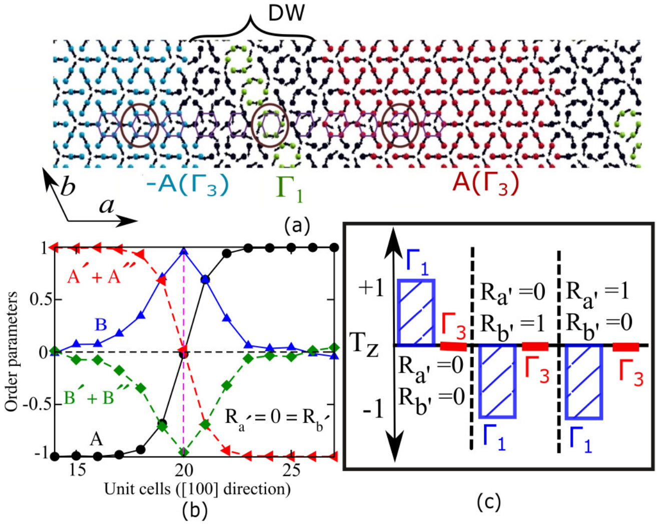

FIG. 3. Stripe domains of antiferromagnetically ordered states obtained from simulations at 4 K: (a) 180° antiferromagnetic domain wall. Hexagon inside the brown circle is used in (a) to represent magnetic ordering according to symmetry of Γ_1 irreducible representation at the 180° domain wall. (b) Variation in local antiferromagnetic order parameters (Γ_1: B, B', and B''; Γ_3: A, A', and A'') across the 180° antiferromagnetic domain wall shows buildup of magnetic ordering of Γ_1 irreducible representation (green) at the domain wall. (c) z component of the toroidal moment (T_z) is calculated with three choices of origins ((i) $R_{a'} = 0 = R_{b'}$ [$R_{a'}$ and $R_{b'}$ are lattice vectors of paraelectric structure; see Fig. 1(a)], (ii) $R_{a'} = 0$, $R_{b'} = 1$, and (iii) $R_{a'} = 1$, $R_{b'} = 0$) from the homogeneous magnetic ordering (bulk crystal) of Γ_3 and Γ_1 irreducible representations. T_z of antiferromagnetic ordering of Γ_1 irreducible representation picks up a phase of π when the origin is translated by $R_{a'}$ or $R_{b'}$. T_z of the antiferromagnetically ordered state corresponding to Γ_3 irreducible representation is zero irrespective of the choice of origin. Vertical dashed lines in (c) separate the values of toroidal moments (T_z) calculated with three choices of origin.

We evaluate local antiferromagnetic order parameters associated with Γ_3 [A, A', and A'', defined in Eq. (1)] and Γ_1 [$B = \frac{1}{6}\sum_{i=1}^{6}(\hat{r}_i \times \hat{s}_i)_z$, $B' = \frac{1}{6}\sum_{i=1}^{6}(-1)^i(\hat{c}_i \times \hat{s}_i)_z$, and $B'' = \frac{1}{6}\sum_{i=1}^{6}(-1)^i(\hat{d}_i \times \hat{s}_i)_z$, where $\hat{r}_i$, $\hat{c}_i$, and $\hat{d}_i$ are defined in Fig. 1(c); see Eq. (1) and Fig. S10(b) in [48]] irreducible representations across the antiferromagnetic domain wall with the choice of origin of the unit cell at $R_{a'} = 0 = R_{b'}$ [$R_{a'}$ and $R_{b'}$ are lattice vectors of paraelectric unit cell, green hexagon in Fig. 1(a)]. The antiferromagnetic order parameter A_Γ [$A = 1$, choice of origin at $R_{a'} = 0 = R_{b'}$; see Fig. 1(a)] linearly depends on A'_Γ and A''_Γ ($A' = -0.5$ and $A'' = -0.5$ with the choice of origin at $R_{a'} = 0 = R_{b'}$ and $A_\Gamma = -A'_\Gamma - A''_\Gamma$; see Sec. II B) when a homogeneous magnetic ordering with the symmetry of Γ_3 irreducible representation is considered. Similarly, antiferromagnetic order parameter B_Γ ($B = 1$, choice of origin at $R_{a'} = 0 = R_{b'}$) linearly depends on B'_Γ and B''_Γ ($B' = -0.5$ and $B'' = -0.5$ with the choice of origin at $R_{a'} = 0 = R_{b'}$ and $B_\Gamma = -B'_\Gamma - B''_\Gamma$; see Fig. S10(b) in [48]) in a homogeneously ordered magnetic state with the symmetry of Γ_1 irreducible representation. Our estimates of the local magnetic order parameter B ($= -B' - B''$) at the 180° antiferromagnetic domain wall is close to 1, whereas the value of A ($= -A' - A''$) remains close to zero [see Fig. 3(b)]. If the origin of the unit cell is shifted by $R_{a'}$, then the value of B'' ($= -B - B'$) is close to one at the antiferromagnetic domain wall, whereas the value of A'' ($= -A - A'$) goes to zero. Therefore, magnetic ordering according to Γ_1 irreducible representation is evident at the antiferromagnetic domain wall irrespective of the choice of origin of the unit cell [see Figs. 3(a) and 3(b)].

There is a symmetry allowed nonzero toroidal moment along the z axis associated with the magnetic ordering according to Γ_1 irreducible representation at the 180° antiferromagnetic domain wall [65]. The toroidal moment is defined as

$$T_z = \frac{1}{6}\sum_{i=1}^{6}(\hat{r}_i \times \hat{s}_i)_z, \tag{5}$$

where $\hat{r}_i$ represents a unit vector along the in-plane projection of position vector of ith Mn atom ($i = 1, \dots, 6$) with respect to the center [$\sum_{i=1}^{6}\hat{r}_i = 0$; see Fig. 1(c)] and s_i is the spin vector of ith Mn atom. It is equivalent to the definition of the magnetic order parameter B associated to Γ_1 irreducible representation (Eq. 1 in [48]). We estimate the z component of toroidal moment [T_z using Eq. (5)] considering homogeneously ordered magnetic states of Γ_3 and Γ_1 irreducible representations. If a Mn sublattice at $z = 0$ (origin of unit cell at $R_{a'} = 0 = R_{b'}$) with magnetic ordering according to Γ_3 irreducible representation is translated by $R_{a'}$ or $R_{b'}$, the direction (see Fig. S10(a) in [48]) of each spin has to rotate by 120° counterclockwise (around the z direction and in the ab plane) to keep the system unchanged upon translation. Therefore, local values of toroidal moments in homogeneously ordered magnetic state with Γ_3 irreducible representation (see Fig. S10(c) in [48]) with three different choices of origins (related by $R_{a'}$ or $R_{b'}$) are

$$\begin{aligned} T_z &= \sin(2n\pi/3),\\ &= 0\ (n = 0,\ R_{a'} = 0,\ R_{b'} = 0),\\ &= 0.86\ (n = 1,\ R_{a'} = 1,\ R_{b'} = 0),\\ &= -0.86\ (n = 2,\ R_{a'} = 0,\ R_{b'} = 1). \end{aligned} \tag{6}$$

Similarly, local values of toroidal moment in a homogeneously ordered magnetic state of Γ_1 irreducible representation (see Fig. S10(d) in [48]) are

$$\begin{aligned} T_z &= \cos(2n\pi/3),\\ &= 1\ (n = 0,\ R_{a'} = 0,\ R_{b'} = 0),\\ &= -0.5\ (n = 1,\ R_{a'} = 1,\ R_{b'} = 0),\\ &= -0.5\ (n = 2,\ R_{a'} = 0,\ R_{b'} = 1). \end{aligned} \tag{7}$$

The toroidization lattice (formed by distributions of toroidal moments; see Fig. S10(c)-S10(d) in [48]) corresponding to Γ_3 irreducible representation is inversion (center of inversion in the paraelectric state) symmetric (see Fig. S10(c) in [48]), whereas it is not in the magnetic state of Γ_1 irreducible representation (see Fig. S10(d) in [48]). Translation of the Mn sublattice at $z = 1/2$ (origin of unit cell at $R_{a'} = 0 = R_{b'}$) by $R_{a'}$ or $R_{b'}$ (see Fig. S10(a) in [48]) with the homogeneously ordered magnetic states according to Γ_3 or Γ_1 irreducible representation results in clockwise rotation of each spin by 120° (around the z axis and in the ab plane) to keep the system unchanged upon translation (counterclockwise rotation of each spin by 120° when the Mn sublattice at $z = 0$ is translated by $R_{a'}$ or $R_{b'}$). Therefore, the changes in the toroidal moment due to translation of the origin by $R_{a'}$ or $R_{b'}$ need to be calculated by considering the displacements of both Mn sublattices at $z = 0$ (counterclockwise rotation of spin by 120°) and at $z = 1/2$ (clockwise rotation of spin by 120°):

$$\begin{aligned} &T_z(\Gamma_3, R_{a'} \neq 0 \text{ or } R_{b'} \neq 0)\\ &\quad = \sin(2\pi/3) + \sin(-2\pi/3) = 0,\\ &T_z(\Gamma_1, R_{a'} \neq 0 \text{ or } R_{b'} \neq 0)\\ &\quad = \cos(2\pi/3) + \cos(-2\pi/3) = -1. \end{aligned} \tag{8}$$

T_z (associated with the magnetic ordering with Γ_1 irreducible representation) picks up a phase of π (toroidization quantum analogous to polarization quantum [66]) under the translation operation by $R_{a'}$ or $R_{b'}$. This is pictorially represented in Fig. 3(c) and highlights that the magnitude of the difference in toroidal moments associated with magnetic states (homogeneously ordered) with Γ_3 and Γ_1 irreducible representations is always unity irrespective of the choice of origin of the unit cell.

Emergence of antiferromagnetic ordering corresponding to Γ_1 irreducible representation at the domain wall separating the domains of antiferromagnetic states with the symmetry of Γ_3 irreducible representation supports its linear coupling with electric field, as allowed by symmetry. Toroidal moment (T_z) is a polar vector that changes sign under spatial inversion and time reversal operations. Symmetries which allow for off-diagonal and antisymmetric components of a linear magnetoelectric tensor are identical to that allowing for a nonzero toroidal moment [66,67]. Thus a toroidal moment couples linearly to the cross product of electric and magnetic fields.

Interactions between ferroelectric polarization (P_z), toroidal moment (T) associated to Γ_1 irreducible representation, applied electric field (E), and magnetic field (H) at the 180° antiferromagnetic domain wall in the low temperature phase ($T < T_N$) can be modeled as

$$\begin{aligned} F(E, P_z, T, H) = {} & \tfrac{1}{2}\epsilon P_z^2 + a_1 T^2 - P_z E_z\\ & + c_1 T_z E_z + c_2 T \cdot (E \times H), \end{aligned} \tag{9}$$

where ϵ is the dielectric susceptibility. The z component of the toroidal moment acts as an antiferromagnetic order parameter corresponding to Γ_1 irreducible representation [see Eq. (5) and Eq. S1]. Noncollinear antiferromagnetic ordering [in the ab plane; see Fig. 3(a) here and Fig. S10(b) in [48]] according to the symmetry of Γ_1 irreducible representation does not respect spatial inversion symmetry. Hence an additional nonzero component of polarization along the z axis is expected along with the one originating from nonlinear coupling between zone boundary and zone center polar phonon modes at the ferroelectric transition [6,30,33] at 1270 K. This particular coupling is modeled through the fourth term in Eq. (9) and is nonzero only at the 180° antiferromagnetic domain wall below T_N. The last term in the right hand side of Eq. (9) represents a trilinear coupling between toroidal moment, electric field, and magnetic field that is compatible with the space and time reversal symmetries. This term gives a nonzero off-diagonal magnetoelectric coupling in any material with a nonzero toroidal moment.

The first derivative of free energy [Eq. (9)] at the antiferromagnetic domain wall with respect to E_z is given as

$$P'_z - P_z = \Delta P_z = -c_1 T_z, \tag{10}$$

which quantifies the change in the spontaneous polarization along the z axis at the antiferromagnetic domain wall due to the nonzero toroidal moment and can be measured in piezoresponse force microscopy experiments. We approximate the change in ferroelectric polarization at the antiferromagnetic domain wall by estimating the difference in bulk polarization (Berry phase) of the two homogeneously ordered magnetic states corresponding to Γ_3 and Γ_1 irreducible representations. The estimated change in bulk polarization is around 3×10^{-2} μC/cm^2. The estimated change in polarization is comparable to the value of magnetically induced ferroelectric polarization in TbMnO$_3$ (8×10^{-2} μC/cm^2) [68] and an order of magnitude larger than that observed in $S = 1/2$ Kagome magnet PbCu$_3$TeO$_7$ (1.4×10^{-3} μC/cm^2) [69], molecular magnet (ND$_4$)$_2$ [FeCl$_5$(D$_2$O)] (3×10^{-4} μC/cm^2) [70], and frustrated magnet MnWO$_4$ (5×10^{-3} μC/cm^2) [71]. The change in polarization at the 180° antiferromagnetic domain wall is even comparable to the ferroelectric polarization measured in improper ferroelectrics (Rb$_2$ZnCl$_4$: 12×10^{-2} μC/cm^2; K$_2$SeO$_4$: 5.6×10^{-2} μC/cm^2) where the primary order parameter is structural [72,73].

The first derivative of free energy [Eq. (9)] at the antiferromagnetic domain wall with respect to E_x and E_y are given as

$$\begin{aligned} P_x &= -\frac{\partial F}{\partial E_x} = -c_2 T_z H_y, \\ P_y &= -\frac{\partial F}{\partial E_y} = c_2 T_z H_x. \end{aligned} \tag{11}$$

The magnetic field along y (x) direction induces ferroelectric polarization along x (y) direction at the 180° domain wall due to a nonzero toroidal moment (T_z) along z direction. This gives rise to the transverse (off-diagonal) linear magnetoelectric effect at the 180° antiferromagnetic domain wall of YMnO$_3$ which is symmetry forbidden in bulk. The linear magnetoelectric effect at the antiferromagnetic domain wall predicted here is magnetic in origin and not induced by structural distortion in contrast to the bulk magnetoelectric effect observed in hexagonal LuFeO$_3$ [74] and ErMnO$_3$ [75]. The linear, transverse magnetoelectric response of the antiferromagnetic domain wall in YMnO$_3$ can be utilized in visualization of the 180° antiferromagnetic domain wall in piezoresponse force microscopy.

E. Antiferromagnetostructural domain wall

We next investigate inhomogeneous spin ordering at the antiferromagnetostructural domain wall (antiferromagnetic states locked to structural states). The six states of coupled antiferromagnetic and structural ordering below T_N [modeled in Eq. (2)] are (a) A_Γ (u_Γ or $-u_\Gamma$), (b) A'_Γ (u'_Γ or $-u'_\Gamma$), (c) A''_Γ (u''_Γ or $-u''_\Gamma$), (d) $-A_\Gamma$ (u_Γ or $-u_\Gamma$), (e) $-A'_\Gamma$ (u'_Γ or $-u'_\Gamma$), and (f) $-A''_\Gamma$ (u''_Γ or $-u''_\Gamma$). Polarization is associated with Γ_1 irreducible representation in the ferroelectric phase ($P6_3cm1'$). u_Γ's ($-u_\Gamma$'s) structural states appear in the ferroelectric phase with positive (negative) value of polarization (see Sec. II A). Due to the third order spin-phonon coupling [last term in Eq. (2)], magnetic state A_Γ (antiferromagnetic ordering) can coexist with both u_Γ and $-u_\Gamma$ structural states. The indirect coupling between antiferromagnetic (A_Γ) and ferroelectric order parameters (P_z) is mediated by the structural order parameter (u_Γ). Thus the structural and ferroelectric domain walls serve also as magnetic domain walls (at $T < T_N$).

We simulate the full model Hamiltonian [Eq. (4)] with a periodic system of $60 \times 60 \times 8$ unit cells to investigate the structure and nature of ordering of spins at the antiferromagnetostructural domain wall (structurally locked antiferromagnetic domains). We now examine the spin configuration equilibrated at 4 K and starting with a stripe ordering of six antiferromagnetic domains [see Fig. 4(b)] in the heating-up simulation [initial state: stripe domain pattern formed by three antiferromagnetic states A_Γ, A'_Γ, and A''_Γ in the ab plane (sequence: $A_\Gamma \rightarrow A'_\Gamma \rightarrow A''_\Gamma$)]. The observed sequence [see Fig. 4(a) and 4(b)] of six antiferromagnetic states in the stripe pattern is $-A'_\Gamma \rightarrow A_\Gamma \rightarrow -A''_\Gamma \rightarrow A'_\Gamma \rightarrow -A_\Gamma \rightarrow A''_\Gamma$. Between the two adjacent antiferromagnetic domains, spins in the $z = 0$ plane ($z = 1/2$ plane) rotate by 60° in the counterclockwise (clockwise) direction [e.g., going from $-A'_\Gamma$ to A_Γ; see Fig. 4(b)] across the antiferromagnetostructural domain wall. These magnetic domain walls are much wider (≈38 Å) than the structural domain walls [6] (5–10 Å) simulated in YMnO$_3$. Such thick domain walls are generally observed in most collinear [76] and noncollinear magnetic materials [77]. Estimated domain wall energy of the 60° antiferromagnetic domain wall is ≈6.8 mJ/m^2 and is higher than that of a 180° magnetic domain wall (4 mJ/m^2). Another possible sequence of antiferromagnetic orderings in the stripe domain structure is $-A'_\Gamma \rightarrow A''_\Gamma \rightarrow -A_\Gamma \rightarrow A'_\Gamma \rightarrow -A''_\Gamma \rightarrow A_\Gamma$, which is symmetry equivalent to the one presented in Fig. 4(a). In this case, spins at $z = 0$ plane ($z = \frac{1}{2}$ plane) rotate by 60° in the clockwise (counterclockwise) direction across the antiferromagnetostructural domain wall [e.g., going from $-A'_\Gamma$ to A''_Γ and see Fig. 4(b)].

Depending on the coupling between structural, ferroelectric, and antiferromagnetic order parameters [Eq. (2)], the choices of structural and ferroelectric ordering in the observed sequence of antiferromagnetic domains in this configuration [see Fig. 4(a)] are (a) $-A'_\Gamma$: $(-u'_\Gamma, -P_z) \rightarrow A_\Gamma$: $(u_\Gamma, P_z) \rightarrow -A''_\Gamma$: $(-u''_\Gamma, -P_z) \rightarrow A'_\Gamma$: $(u'_\Gamma, P_z) \rightarrow -A_\Gamma$: $(-u_\Gamma, -P_z) \rightarrow A''_\Gamma$: (u''_Γ, P_z) or (b) $-A'_\Gamma$: $(u'_\Gamma, P_z) \rightarrow A_\Gamma$: $(-u_\Gamma, -P_z) \rightarrow -A''_\Gamma$: $(u''_\Gamma, P_z) \rightarrow A'_\Gamma$: $(-u'_\Gamma, -P_z) \rightarrow -A_\Gamma$: $(u_\Gamma, P_z) \rightarrow A''_\Gamma$: $(-u''_\Gamma, -P_z)$. Change in the antiferromagnetic ordering across a magnetostructural domain wall causes change in the structural ordering, which causes the locking between antiferromag-

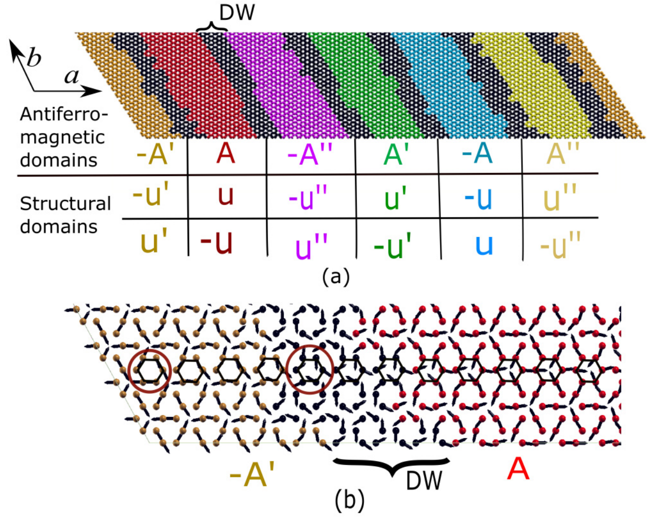

FIG. 4. (a) Stripe pattern of antiferromagnetic domains with spin direction changing by 60° at 4 K coupled to structural domains (antiferromagnetostructural domain wall or 60° antiferromagnetic domain wall). The structural domain corresponding to each magnetic domain is listed in (a). There are two choices of ordering of structural domains due to third order spin-phonon coupling. Both choices involve rotation of atomic displacement vectors (in the *ab* plane) by 60° (O2 atoms: counterclockwise rotation going from $-u'_\Gamma$ to u_Γ or u'_Γ to $-u_\Gamma$) across the domain wall. A magnetostructural domain wall separating $-u'_\Gamma$ and $-u_\Gamma$ corresponding to change in the trimerization angle by $2\pi/3$ (no change in sign of P_z) has not been observed experimentally [6,37]. (b) Atomic scale structure of ordering of spins across the 60° domain wall separating antiferromagnetic states $-A'_\Gamma$ and A_Γ. Hexagon inside the red circle in (b) is used to represent the choice of origin [$R_{a'} = 0 = R_{b'}$, where $R_{a'}$ and $R_{b'}$ are lattice vectors of paraelectric structure; see Fig. 1(a)] and the magnetic order parameters A's are estimated with this choice of origin. In each magnetic domain, the local value of the antiferromagnetic order parameter is larger than 0.93. Black colored portions in (a) denote a 60° antiferromagnetic domain wall.

netic states and structural states (as discussed earlier in this subsection). Atomic displacement vectors (O1 atoms at $z = 0.16$) rotate by 60° in the clockwise (counterclockwise for O2 atoms at $z = 0.33$) direction [see Fig. 1(b)] between two consecutive magnetostructural domains (e.g., from $-A'_\Gamma$ to A_Γ) and are in agreement with earlier theoretical analysis [6]. The antiferromagnetostructural domain wall separating structural states $-u'_\Gamma$ and $-u_\Gamma$ corresponds to a change in trimerization angle by $2\pi/3$ [see Fig. 4(a)]. This particular antiferromagnetostructural domain wall separating structural states ($-u'_\Gamma$ and $-u_\Gamma$; $-P_z$) with the same sign of polarization has not been observed experimentally [38]. Earlier first-principles calculations [6,37] have shown that this type of magnetostructural domain wall is not energetically favorable and decays into the lowest energy ferroelectric and structural domain walls across which atomic displacement vectors rotate by 60° [60° domain wall; see Fig. 4(a)].

F. Magnetic topological defects

Motivated by structural topological defects in Ref. [6], we now present analysis of magnetic topological defects [see Figs. 5(a) and 5(b)]. A topological defect arises at the intersection of six 60° antiferromagnetic domain walls [see Figs. 5(a) and 5(b)]. Spins in the neighboring antiferromagnetic domains [A'_Γ to $-A''_\Gamma$ in Fig. 5(c)] at the $z = 0$ plane ($z = 1/2$ plane) rotate by 60° in the clockwise (counterclockwise) direction in the vortex state, whereas this is reversed in the antivortex state. We label such cyclic ordering of six antiferromagnetic domains [see Figs. 5(a) and 5(b)] as Z_6 vortex as spins rotate by 60° across a domain wall. In contrast to the commonly observed magnetic vortices [78], a vortex in YMnO$_3$ does not contain a core (central singularity) in which spins point parallel to the vortex line [78]. We define a topological charge (Q_T) to differentiate a magnetic vortex from an antivortex state:

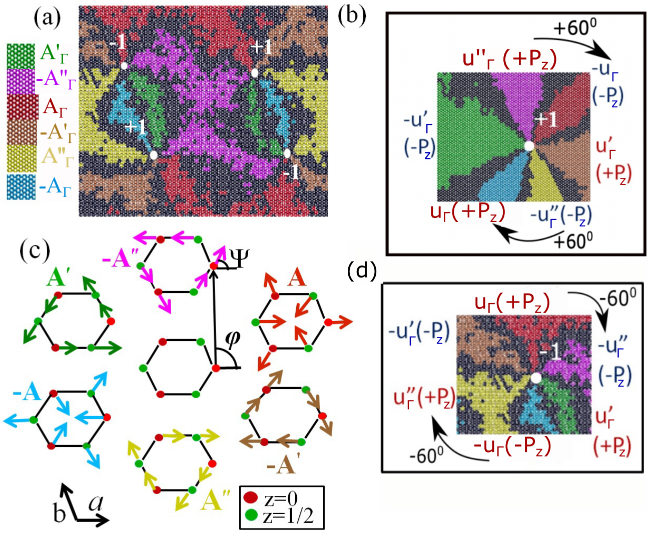

FIG. 5. Antiferromagnetic vortex and antivortex states obtained in systems simulated with (a) periodic boundary conditions and (b) open boundary conditions. +1 and −1 are the topological charges associated with antiferromagnetic vortex and antivortex states. Black colored regions in (a), (b), and (d) denote antiferromagnetic domain walls. (c) Atomic scale schematic ordering of spins in the core of a vortex corresponding to (b). Ψ (φ) in (c) represents the azimuthal angle enclosed by the direction of spin (position vector of an Mn atom with respect to the vortex core) with *a* axis. Panels (b) and (d) represent orderings of structural states in the core of the magnetic vortex and antivortex, respectively. Displacement vectors associated with O2 atoms across the antiferromagnetostructural domain wall in (b) separating u''_Γ and $-u_\Gamma$ rotate by 60° in a clockwise direction. Similarly, displacement vectors associated with O2 atoms across the antiferromagnetostructural domain wall in (d) separating u_Γ and $-u''_\Gamma$ rotate by 60° in a counterclockwise direction. Panels (b) and (d) represent structural vortex and antivortex states.

$$\begin{aligned} Q_T &= \frac{1}{4\pi}\left[\oint_{z=0}\frac{\partial\Psi}{\partial\varphi}\,d\varphi - \oint_{z=1/2}\frac{\partial\Psi}{\partial\varphi}\,d\varphi\right],\\ &= \frac{1}{4\pi}\left[\Psi_{z=0}\big|_{\varphi=0}^{\varphi=2\pi} - \Psi_{z=1/2}\big|_{\varphi=0}^{\varphi=2\pi}\right],\\ &= \frac{1}{4\pi}\times 4\pi m \quad [\Psi = m\varphi + \gamma],\\ &= m, \end{aligned} \tag{12}$$

where Ψ (φ) represents the azimuthal angle enclosed by the direction of spin (position vector of Mn atom with respect to the vortex core) with a axis [see Fig. 5(c)]. The helicity of the spin texture is defined by the phase γ [79,80]. m is the vorticity and its value is $+1$ in the vortex state and -1 in the antivortex state and their corresponding topological charges (Q_T) are $+1$ and -1. Our definition of topological charge is equivalent to the definition of vorticity of an in-plane spin texture of magnetic skyrmions [79,80]. The net topological charge (Q_T) in a periodic system vanishes, whereas it can be nonzero with open boundary conditions [see Figs. 5(a) and 5(b)]. We estimate the antiferromagnetostructural vortex energy density using

$$\epsilon_{\text{vortex}} = \frac{E^{\text{OBC}}_{\text{vortex}} - E^{\text{OBC}}_{\text{single}} - 6S \times \epsilon^{60^\circ}_{DW}}{L_v}. \tag{13}$$

$E^{\text{OBC}}_{\text{vortex}}$ and $E^{\text{OBC}}_{\text{single}}$ are the energies of a system containing a vortex and of a single antiferromagnetic domain calculated with open boundary conditions, respectively. S is the total area of a domain wall and L_v is the length of the vortex line along the z axis. $\epsilon^{60^\circ}_{DW}$ is the energy of the antiferromagnetostructural domain wall across which spins rotate by 60° [see Fig. 4(a)]. The vortex energy considers both the magnetic and structural degrees of freedom through the phonon renormalized spin Hamiltonian [Eq. (4)] as compared to earlier works based on a structural model Hamiltonian which focused on understanding the evolution of crystal structure and formation of structural vortex near a ferroelectric transition [81,82]. Our estimate of the vortex energy using Eq. (13) is 70×10^{-10} J/m, which is of the same order as the dislocation energy in Cu [30×10^{-10} J/m, shear modulus (G) = 45 GPa at 300 K [83,84]]. Due to the locking of antiferromagnetic states to structural states (as discussed earlier), the magnetic vortex (antivortex) state corresponds to the structural vortex (antivortex) state. In the structural vortex (antivortex) state, displacement vectors associated with O2 atoms ($z = 0.33$) rotate in the clockwise (counterclockwise) direction by 60° [see Figs. 5(b) and 5(d)] across a boundary between neighboring structural domains.

Atomic displacements associated with Γ_1 phonon mode [u_Γ, u'_Γ, and u''_Γ; see Fig. 1(b)] of ferroelectric $P6_3cm1'$ phase are symmetry equivalent to the polar K_3 (with trimerization angle $\Phi = 0, 2\pi/3$, and $-2\pi/3$; see Fig. S1(a)-S1(c) in [48]) and Γ_2^- (P_z) phonon modes of paraelectric $P6_3/mmc1'$ phase (see Sec. II A). Six structural states below T_N in terms of trimerization angle Φ (associated with K_3 phonon mode) are defined [6] as (a) $u_\Gamma \leftrightarrow (\Phi = 0, +P_z)$, (b) $-u_\Gamma \leftrightarrow (\Phi = \pi, -P_z)$, (c) $u'_\Gamma \leftrightarrow (\Phi = 2\pi/3, P_z)$, (d) $-u'_\Gamma \leftrightarrow (\Phi = -\pi/3, -P_z)$, (e) $u''_\Gamma \leftrightarrow (\Phi = -2\pi/3, +P_z)$, and (f) $-u''_\Gamma \leftrightarrow (\Phi = \pi/3, -P_z)$. A sequence of cyclic ordering of structural domains [see Figs. 5(b), 5(d) and 1(c) here and Fig. S1(a)-S1(c) in [48]] around the vortex line (in the clockwise direction) in terms of Φ (trimerization angle) is $\Phi = 0\ (u_\Gamma) \rightarrow -\pi/3\ (-u'_\Gamma) \rightarrow -2\pi/3\ (u''_\Gamma) \rightarrow \pi (-u_\Gamma) \rightarrow 2\pi/3\ (u'_\Gamma) \rightarrow \pi/3\ (-u''_\Gamma)$. In the antivortex state, the sequence is $\Phi = 0\ (u_\Gamma) \rightarrow \pi/3\ (-u''_\Gamma) \rightarrow 2\pi/3\ (u'_\Gamma) \rightarrow \pi\ (-u_\Gamma) \rightarrow -2\pi/3\ (u''_\Gamma) \rightarrow -\pi/3\ (-u'_\Gamma)$. Angle Φ [see Figs. S1(a)-S1(c) and Fig. S11 in [48], and Figs. 5(b) and 5(d) here] changes clockwise (counterclockwise) across the domain wall in the vortex (antivortex) state and is consistent with the experimental findings [38–40]. The sign of ferroelectric polarization changes across a magnetostructural domain wall (similar to the case of a 60° domain wall in stripe pattern formed by antiferromagnetic domains). Our predictions of the orderings of structural and ferroelectric domains (in the vortex and antivortex states) below T_N are in agreement with earlier theoretical analysis [6] and experimental work [38,39].

III. SUMMARY

Using statistical mechanical analysis of the first-principles spin-phonon coupled Hamiltonian of $YMnO_3$, we established that confinement of spins in the ***ab*** plane and their ordering according to Γ_3 irreducible representation below T_N induces nonzero atomic displacements associated to Γ_1 irreducible representation as the secondary order parameter. The Néel transition is weakly first order or close to being second order in nature and our estimates of T_N and θ_{CW} are in reasonable agreement with their experimental values. We predict that the 180° antiferromagnetic domain wall within a single structural domain involves local ordering of spins according to the symmetry of Γ_1 irreducible representation and hence hosts a local linear magnetoelectric coupling. This finding provides a deeper understanding of the magnetoelectric effects at antiferromagnetic domain walls and will encourage experimental confirmation using piezoresponse force microscopy. We highlight that antiferromagnetic domains are locked to the structural and ferroelectric domains. With spins and atomic displacements rotating by 60° across a boundary between adjacent domains, an antiferromagnetic vortex state with nontrivial topological charge is stabilized. Thus antiferromagnetic domain walls offer a new playground to explore emergent interfacial phenomena and future understanding of their dynamic responses to external stimuli is desirable for advancing antiferromagnetic spintronic technologies based on antiferromagnetic materials. There remains an open issue of underestimation of amplitude of the K_1 phonon mode, i.e., position of Mn atom below T_N, and it is possible that including the effects of dynamical electronic correlations and quantum spin fluctuations might resolve this discrepancy with experiment. While studies of these effects are beyond the scope of the present article, we believe that the work in this direction will also impact understanding of magnetically frustrated systems which show magnetoelastic effects.

IV. METHODS

We optimized atomic positions of $YMnO_3$ within first-principles density functional theory as implemented in the QUANTUM ESPRESSO package [85] and treated spin dependent exchange-correlation energy within a local density approximation (LDA) in the Perdew-Zunger parametrized functional [86]. We used fully relativistic pseudopotentials [87] to include the effects of spin-orbit coupling (SOC) in determination of all the parameters in our model Hamiltonian. We employed the Berry phase method [88] as implemented in QUANTUM ESPRESSO [85] to estimate the difference in polarization of bulk $YMnO_3$ with magnetic moments ordered in the *ab* plane according to Γ_1 and Γ_3 irreducible representations (see Sec. D in [48] for more details).

We performed classical Monte Carlo simulations on a model Hamiltonian [Eq. (4) in the main text] to determine the behaviors of antiferromagnetic and structural order parameters in $\mathrm{YMnO_3}$ near the Néel transition. In these simulations, we considered a supercell with each hexagonal unit cell containing six Mn atoms. The in-plane positions of Mn atoms form an ideal triangular lattice. The direction of Heisenberg spin at ith Mn site is defined by ($\theta_i \in [0, \pi]$, $\phi_i \in [0, 2\pi]$) and it is updated by randomly choosing $\theta_i = \cos^{-1}(2u - 1)$ and $\phi_i = 2v$, where u and v are pseudorandom random numbers (uniformly distributed between 0 and 1). The updated direction of spin (θ_i, ϕ_i) is accepted by following the standard Metropolis algorithm. We considered periodic systems of 9 × 9 × 9 (single structural domain) and 60 × 60 × 8 unit cells (multiple structural and magnetic domains) and carried out heating-up and cooling-down simulations with temperature steps of ±2 K. We used 90 000 Monte Carlo steps for thermalization followed by 90 000 Monte Carlo steps for statistical averaging of various properties at each temperature. We chose a randomly generated spin configuration as the initial state in cooling-down simulations and spin configuration with Γ_3 irreducible representation as the initial state in heating-up simulations. Average values of antiferromagnetic order parameters (A, A', A'', and M) at each temperature are estimated using

$$\begin{aligned} A(T) &= \frac{1}{U \times N_{\mathrm{ave}}} \sum_{j=1}^{N_{\mathrm{ave}}} \sum_{n=1}^{U} |A_{n,j}|, \\ A'(T) &= \frac{1}{U \times N_{\mathrm{ave}}} \sum_{j=1}^{N_{\mathrm{ave}}} \sum_{n=1}^{U} |A'_{n,j}|, \\ A''(T) &= \frac{1}{U \times N_{\mathrm{ave}}} \sum_{j=1}^{N_{\mathrm{ave}}} \sum_{n=1}^{U} |A''_{n,j}|, \\ M(T) &= \frac{1}{U \times N_{\mathrm{ave}}} \sum_{j=1}^{N_{\mathrm{ave}}} \sum_{n=1}^{U} |M_{n,j}|. \end{aligned} \tag{14}$$

N_{ave} denotes the number of Monte Carlo steps used in thermal averaging and U is the total number of unit cells. Here $|A_{n,j}|$ ($|M_{n,j}|$) is the absolute value of the order parameter A (M) associated with nth unit cell in the jth spin configuration. We calculated average values of A' and A'' in a similar way of calculating the value of A. Generalized magnetic susceptibility associated with the phase transition and specific heat are

$$\begin{aligned} \chi_{ab} &= \frac{1}{2}(\chi_a + \chi_b), \\ \chi_a &= \frac{\langle M_{Fx}^2 \rangle - \langle M_{Fx} \rangle^2}{k_B T}, \\ \chi_b &= \frac{\langle M_{Fy}^2 \rangle - \langle M_{Fy} \rangle^2}{k_B T}, \\ M_{Fx(y)}(T) &= \frac{1}{6U \times N_{\mathrm{ave}}} \sum_{j=1}^{N_{\mathrm{ave}}} \sum_{i=1}^{6U} s_{x(y),ij}(T), \\ M_{Fx}^2(T) &= \frac{1}{6U \times N_{\mathrm{ave}}} \sum_{j=1}^{N_{\mathrm{ave}}} M_{Fx,j}^2(T), \\ C_V &= \frac{\langle E^2 \rangle - \langle E \rangle^2}{k_B T^2}, \quad \text{where } \langle E \rangle = \frac{1}{N_{\mathrm{ave}}} \sum_{j=1}^{N_{\mathrm{ave}}} E_j, \end{aligned} \tag{15}$$

where E_j is the energy of the jth configuration of spins. To determine the magnetic topological defects, we carried out heating-up Monte Carlo simulations (initial state: vortex configuration consisting of six antiferromagnetic states A, A', A'', $-A$, $-A'$, and $-A''$) with open and periodic boundary conditions (on a 60 × 60 × 8 supercell).

All the data supporting the present work are available from the first author upon request.

ACKNOWLEDGMENTS

A.P. is thankful for the support of the research fellowship from the Department of Science and Technology of the Government of India. U.V.W. acknowledges support from a J C Bose National Fellowship from SERB, the Department of Science and Technology of the Government of India. We also acknowledge the support from Shell-Bangalore, India.

U.V.W. planned the project. First-principles and Monte Carlo simulations were performed by A.P. Both authors analyzed the results and contributed to the writing of the manuscript.

The authors declare no competing interests.

---

[1] E. du Trémolet de Lacheisserie, D. Gignoux, and M. Schlenker, *Magnetism* (Springer-Verlag, New York, 2005).

[2] L. Frąckowiak, P. Kuświk, G. D. Chaves-O'Flynn, M. Urbaniak, M. Matczak, P. P. Michałowski, A. Maziewski, M. Reginka, A. Ehresmann, and F. Stobiecki, Phys. Rev. Lett. **124**, 047203 (2020).

[3] S. S. P. Parkin, M. Hayashi, and L. Thomas, Science **320**, 190 (2008).

[4] C. Kittel, Rev. Mod. Phys. **21**, 541 (1949).

[5] C. Mitsumata and A. Sakuma, IEEE Trans. Magn. **47**, 3501 (2011).

[6] S. Artyukhin, K. T. Delaney, N. A. Spaldin, and M. Mostovoy, Nat. Mater. **13**, 42 (2014).

[7] K. Kuroda, T. Tomita, M.-T. Suzuki, C. Bareille, A. A. Nugroho, P. Goswami, M. Ochi, M. Ikhlas, M. Nakayama, S. Akebi, R. Noguchi, R. Ishii, N. Inami, K. Ono, H. Kumigashira, A. Varykhalov, T. Muro, T. Koretsune, R. Arita, S. Shin, T. Kondo, and S. Nakatsuji, Nat. Mater. **16**, 1090 (2017).

[8] S. Nakatsuji, N. Kiyohara, and T. Higo, Nature (London) **527**, 212 (2015).

[9] D. Zhang, M. Shi, T. Zhu, D. Xing, H. Zhang, and J. Wang, Phys. Rev. Lett. **122**, 206401 (2019).

[10] I. Felner, I. Nowik, E. R. Bauminger, D. Hechel, and U. Yaron, Phys. Rev. Lett. **65**, 1945 (1990).

[11] P. Rosa, Y. Xu, M. Rahn, J. Souza, S. Kushwaha, L. Veiga, A. Bombardi, S. Thomas, M. Janoschek, E. Bauer, M. Chan, Z. Wang, J. Thompson, N. Harrison, P. Pagliuso, A. Bernevig, and F. Ronning, npj Quantum Mater. **5**, 52 (2020).

[12] S. Sachdev, Science **336**, 1510 (2012).

[13] X. F. Lu, N. Z. Wang, H. Wu, Y. P. Wu, D. Zhao, X. Z. Zeng, X. G. Luo, T. Wu, W. Bao, G. H. Zhang, F. Q. Huang, Q. Z. Huang, and X. H. Chen, Nat. Mater. **14**, 325 (2015).

[14] E. G. Tveten, A. Qaiumzadeh, and A. Brataas, Phys. Rev. Lett. **112**, 147204 (2014).

[15] T. Shiino, S.-H. Oh, P. M. Haney, S.-W. Lee, G. Go, B.-G. Park, and K.-J. Lee, Phys. Rev. Lett. **117**, 087203 (2016).

[16] T. Jungwirth, X. Marti, P. Wadley, and J. Wunderlich, Nature Nanotech. **11**, 231 (2016).

[17] J. M. Logan, H. C. Kim, D. Rosenmann, Z. Cai, R. Divan, O. G. Shpyrko, and E. D. Isaacs, Appl. Phys. Lett. **100**, 192405 (2012).

[18] M. Bode, E. Y. Vedmedenko, K. von Bergmann, A. Kubetzka, P. Ferriani, S. Heinze, and R. Wiesendanger, Nat. Mater. **5**, 477 (2006).

[19] O. G. Shpyrko, E. D. Isaacs, J. M. Logan, Y. Feng, G. Aeppli, R. Jaramillo, H. C. Kim, T. F. Rosenbaum, P. Zschack, M. Sprung, S. Narayanan, and A. R. Sandy, Nature (London) **447**, 68 (2007).

[20] S.-W. Cheong, M. Fiebig, W. Wu, L. Chapon, and V. Kiryukhin, npj Quantum Mater. **5**, 3 (2020).

[21] D. Meier, J. Seidel, A. Cano, K. Delaney, Y. Kumagai, M. Mostovoy, N. A. Spaldin, R. Ramesh, and M. Fiebig, Nat. Mater. **11**, 284 (2012).

[22] W. Wu, Y. Horibe, N. Lee, S.-W. Cheong, and J. R. Guest, Phys. Rev. Lett. **108**, 077203 (2012).

[23] G. Catalan, J. Seidel, R. Ramesh, and J. F. Scott, Rev. Mod. Phys. **84**, 119 (2012).

[24] C.-L. Jia, S.-B. Mi, K. Urban, I. Vrejoiu, M. Alexe, and D. Hesse, Nat. Mater. **7**, 57 (2008).

[25] J. Seidel, L. W. Martin, Q. He, Q. Zhan, Y.-H. Chu, A. Rother, M. E. Hawkridge, P. Maksymovych, P. Yu, M. Gajek, N. Balke, S. V. Kalinin, S. Gemming, F. Wang, G. Catalan, J. F. Scott, N. A. Spaldin, J. Orenstein, and R. Ramesh, Nat. Mater. **8**, 229 (2009).

[26] J. Matsuno, N. Ogawa, K. Yasuda, F. Kagawa, W. Koshibae, N. Nagaosa, Y. Tokura, and M. Kawasaki, Sci. Adv. **2**, e1600304 (2016).

[27] X. Z. Yu, Y. Onose, N. Kanazawa, J. H. Park, J. H. Han, Y. Matsui, N. Nagaosa, and Y. Tokura, Nature (London) **465**, 901 (2010).

[28] W. J. Kim, J. H. Gruenewald, T. Oh, S. Cheon, B. Kim, O. B. Korneta, H. Cho, D. Lee, Y. Kim, M. Kim, J.-G. Park, B.-J. Yang, A. Seo, and T. W. Noh, Phys. Rev. B **98**, 125103 (2018).

[29] Y. Geng, N. Lee, Y. J. Choi, S.-W. Cheong, and W. Wu, Nano Lett. **12**, 6055 (2012).

[30] B. B. VanAken, T. T. Palstra, A. Filippetti, and N. A. Spaldin, Nat. Mater. **3**, 164 (2004).

[31] S.-W. Cheong and M. Mostovoy, Nat. Mater. **6**, 13 (2007).

[32] B. G. Ueland, J. W. Lynn, M. Laver, Y. J. Choi, and S.-W. Cheong, Phys. Rev. Lett. **104**, 147204 (2010).

[33] C. J. Fennie and K. M. Rabe, Phys. Rev. B **72**, 100103(R) (2005).

[34] X. Fabrèges, S. Petit, I. Mirebeau, S. Pailhès, L. Pinsard, A. Forget, M. T. Fernandez-Diaz, and F. Porcher, Phys. Rev. Lett. **103**, 067204 (2009).

[35] F. Ye, Y. Ren, Q. Huang, J. A. Fernandez-Baca, P. Dai, J. W. Lynn, and T. Kimura, Phys. Rev. B **73**, 220404(R) (2006).

[36] S. Lee, A. Pirogov, M. Kang, K.-H. Jang, M. Yonemura, T. Kamiyama, S.-W. Cheong, F. Gozzo, N. Shin, H. Kimura, Y. Noda, and J.-G. Park, Nature (London) **451**, 805 (2008).

[37] Y. Kumagai and N. A. Spaldin, Nat. Commun. **4**, 1540 (2013).

[38] T. Choi, Y. Horibe, H. T. Yi, Y. J. Choi, W. Wu, and S.-W. Cheong, Nat. Mater. **9**, 253 (2010).

[39] S. C. Chae, Y. Horibe, D. Y. Jeong, S. Rodan, N. Lee, and S.-W. Cheong, Proc. Natl. Acad. Sci. USA **107**, 21366 (2010).

[40] Q. Zhang, G. Tan, L. Gu, Y. Yao, C. Jin, Y. Wang, X. Duan, and R. Yu, Sci. Rep. **3**, 2741 (2013).

[41] T. Matsumoto, R. Ishikawa, T. Tohei, H. Kimura, Q. Yao, H. Zhao, X. Wang, D. Chen, Z. Cheng, N. Shibata, and Y. Ikuhara, Nano Lett. **13**, 4594 (2013).

[42] D. R. Småbråten, Q. N. Meier, S. H. Skjærvø, K. Inzani, D. Meier, and S. M. Selbach, Phys. Rev. Mater. **2**, 114405 (2018).

[43] A. Muñoz, J. A. Alonso, M. J. Martínez-Lope, M. T. Casáis, J. L. Martínez, and M. T. Fernández-Díaz, Phys. Rev. B **62**, 9498 (2000).

[44] J. Park, M. Kang, J. Kim, S. Lee, K.-H. Jang, A. Pirogov, J.-G. Park, C. Lee, S.-H. Park, and H. C. Kim, Phys. Rev. B **79**, 064417 (2009).

[45] A. Paul, P. Sharma, and U. V. Waghmare, Phys. Rev. B **92**, 054106 (2015).

[46] H. T. Stokes, B. J. Campbell, and D. M. Hatch, Isotropy software suite, iso.byu.edu.

[47] H. Wang, I. V. Solovyev, W. Wang, X. Wang, P. J. Ryan, D. J. Keavney, J.-W. Kim, T. Z. Ward, L. Zhu, J. Shen, X. M. Cheng, L. He, X. Xu, and X. Wu, Phys. Rev. B **90**, 014436 (2014).

[48] See Supplemental Material at http://link.aps.org/supplemental/10.1103/PhysRevB.107.174403 for atomic displacements of nonpolar K_1 and polar K_3 phonon modes, details on the first-principles calculations for estimating spin-phonon coupling parameter α and its effect on Néel transition, and the distribution of toroidal moment T_z.

[49] T. N. Tošic, Q. N. Meier, and N. A. Spaldin, Phys. Rev. Res. **4**, 033204 (2022).

[50] A. Prikockytė, D. Bilc, P. Hermet, C. Dubourdieu, and P. Ghosez, Phys. Rev. B **84**, 214301 (2011).

[51] S. Lee, A. Pirogov, J. H. Han, J.-G. Park, A. Hoshikawa, and T. Kamiyama, Phys. Rev. B **71**, 180413(R) (2005).

[52] I. V. Solovyev, M. V. Valentyuk, and V. V. Mazurenko, Phys. Rev. B **86**, 054407 (2012).

[53] T. Katsufuji, S. Mori, M. Masaki, Y. Moritomo, N. Yamamoto, and H. Takagi, Phys. Rev. B **64**, 104419 (2001).

[54] K. A. Ross, L. Savary, B. D. Gaulin, and L. Balents, Phys. Rev. X **1**, 021002 (2011).

[55] T. J. Sato, S. H. Lee, T. Katsufuji, M. Masaki, S. Park, J. R. D. Copley, and H. Takagi, Phys. Rev. B **68**, 014432 (2003).

[56] A. Paul and T. Birol, Phys. Rev. Res. **2**, 033156 (2020).

[57] T. Faske, I. A. Radulov, M. Hölzel, O. Gutfleisch, and W. Donner, J. Phys.: Condens. Matter **32**, 115802 (2020).

[58] I. Shigeta, Y. Fujimoto, R. Ooka, Y. Nishisako, M. Tsujikawa, R. Y. Umetsu, A. Nomura, K. Yubuta, Y. Miura, T. Kanomata, M. Shirai, J. Gouchi, Y. Uwatoko, and M. Hiroi, Phys. Rev. B **97**, 104414 (2018).

[59] P. Marton, I. Rychetsky, and J. Hlinka, Phys. Rev. B **81**, 144125 (2010).

[60] N. B. Weber, H. Ohldag, H. Gomonaj, and F. U. Hillebrecht, Phys. Rev. Lett. **91**, 237205 (2003).

[61] M. S. Wörnle, P. Welter, M. Giraldo, T. Lottermoser, M. Fiebig, P. Gambardella, and C. L. Degen, Phys. Rev. B **103**, 094426 (2021).

[62] S. J. Lloyd, N. D. Mathur, J. C. Loudon, and P. A. Midgley, Phys. Rev. B **64**, 172407 (2001).

[63] A. Scholl, M. Liberati, E. Arenholz, H. Ohldag, and J. Stöhr, Phys. Rev. Lett. **92**, 247201 (2004).

[64] J. Padilla, W. Zhong, and D. Vanderbilt, Phys. Rev. B **53**, R5969(R) (1996).

[65] S. V. Gallego, J. Etxebarria, L. Elcoro, E. S. Tasci, and J. M. Perez-Mato, Acta Crystallogr. Sec. A **75**, 438 (2019).

[66] C. Ederer and N. A. Spaldin, Phys. Rev. B **76**, 214404 (2007).

[67] N. A. Spaldin, M. Fechner, E. Bousquet, A. Balatsky, and L. Nordström, Phys. Rev. B **88**, 094429 (2013).

[68] T. Kimura, T. Goto, H. Shintani, K. Ishizaka, T. Arima, and Y. Tokura, Nature (London) **426**, 55 (2003).

[69] K. Yoo, B. Koteswararao, J. Kang, A. Shahee, W. Nam, F. F. Balakirev, V. S. Zapf, N. Harrison, A. Guda, N. Ter-Oganessian, and K. H. Kim, npj Quantum Mater. **3**, 45 (2018).

[70] J. A. Rodríguez-Velamazán, Ó. Fabelo, Á. Millán, J. Campo, R. D. Johnson, and L. Chapon, Sci. Rep. **5**, 14475 (2015).

[71] K. Taniguchi, N. Abe, T. Takenobu, Y. Iwasa, and T. Arima, Phys. Rev. Lett. **97**, 097203 (2006).

[72] S. Sawada, Y. Shiroishi, A. Yamamoto, M. Takashige, and M. Matsuo, J. Phys. Soc. Jpn. **43**, 2099 (1977).

[73] K. Aiki, K. Hukuda, and O. Matumura, J. Phys. Soc. Jpn. **26**, 1064 (1969).

[74] H. Das, A. L. Wysocki, Y. Geng, W. Wu, and C. J. Fennie, Nat. Commun. **5**, 2998 (2014).

[75] M. Giraldo, Q. N. Meier, A. Bortis, D. Nowak, N. A. Spaldin, M. Fiebig, M. C. Weber, and T. Lottermoser, Nat. Commun. **12**, 3093 (2021).

[76] K. Arai, T. Okuda, A. Tanaka, M. Kotsugi, K. Fukumoto, T. Ohkochi, T. Nakamura, T. Matsushita, T. Muro, M. Oura, Y. Senba, H. Ohashi, A. Kakizaki, C. Mitsumata, and T. Kinoshita, Phys. Rev. B **85**, 104418 (2012).

[77] S. Farokhipoor, C. Magén, S. Venkatesan, J. Íñiguez, C. J. M. Daumont, D. Rubi, E. Snoeck, M. Mostovoy, C. de Graaf, A. Müller, M. Döblinger, C. Scheu, and B. Noheda, Nature (London) **515**, 379 (2014).

[78] A. Hoffmann and H. Schultheiß, Curr. Opin. Solid State Mater. Sci. **19**, 253 (2015).

[79] N. Nagaosa and Y. Tokura, Nat. Nanotechnol. **8**, 899 (2013).

[80] X. Zhang, Y. Zhou, K. M. Song, T.-E. Park, J. Xia, M. Ezawa, X. Liu, W. Zhao, G. Zhao, and S. Woo, J. Phys.: Condens. Matter **32**, 143001 (2020).

[81] S. H. Skjærvø, Q. N. Meier, M. Feygenson, N. A. Spaldin, S. J. L. Billinge, E. S. Bozin, and S. M. Selbach, Phys. Rev. X **9**, 031001 (2019).

[82] M. Lilienblum, T. Lottermosern, S. Manz, S. M. Selbach, A. Cano, and M. Fiebig, Nat. Phys. **11**, 1070 (2015).

[83] M.-H. Nadal and P. Le Poac, J. Appl. Phys. **93**, 2472 (2003).

[84] V. M. Polovov, C. V. Kopetskii, G. I. Kulesko, and V. N. Matveev, Phys. Status Solidi A **11**, 421 (1972).

[85] P. Giannozzi, S. Baroni, N. Bonini, M. Calandra, R. Car, C. Cavazzoni, D. Ceresoli, G. L. Chiarotti, M. Cococcioni, I. Dabo, A. D. Corso, S. de Gironcoli, S. Fabris, G. Fratesi, R. Gebauer, U. Gerstmann, C. Gougoussis, A. Kokalj, M. Lazzeri, L. Martin-Samos, N. Marzari, F. Mauri, R. Mazzarello, S. Paolini, A. Pasquarello, L. Paulatto, C. Sbraccia, S. Scandolo, G. Sclauzero, A. P. Seitsonen, A. Smogunov, P. Umari, and R. M. Wentzcovitch, J. Phys.: Condens. Matter **21**, 395502 (2009).

[86] J. P. Perdew and A. Zunger, Phys. Rev. B **23**, 5048 (1981).

[87] A. Dal Corso and A. Mosca Conte, Phys. Rev. B **71**, 115106 (2005).

[88] R. D. King-Smith and D. Vanderbilt, Phys. Rev. B **47**, 1651 (1993).